



Uniaxial Cyclic and Tensile Tests on Structural Metallic Materials

Alexander R. Hartloper¹; Selimcan Ozden²; Albano de Castro e Sousa³; and Dimitrios G. Lignos, M.ASCE⁴

Abstract: Experimental data is imperative to characterize the behavior of materials used in structural analysis models. The aim of this data paper is to establish a database of material-scale uniaxial experiments, primarily conducted at EPFL, to assist with simulating the monotonic and cyclic behavior of structural steel materials and components. The proposed database consists of stress-strain data from test specimens subjected to tensile straining or to one of nine cyclic load protocols consistent with earthquake loading. The database includes 353 experiments on test specimens fabricated from 11 steel materials from around the world and an iron-based shape memory alloy; the database will evolve as additional tests are conducted. A downsampling method is developed that ensures a difference in strain energy of less than 0.5% between the original and downsampled data while reducing the number of datapoints by 89 times, on average. Results for S355 steels, constituting 57% of the database, are quantitatively validated by comparing the average measured initial yield stress and elastic modulus with prior work. The initial yield stress for S355 steels is found to be between 305 and 430 MPa and the elastic modulus between 190 and 230 GPa; these results are consistent with prior values. Finally, examples illustrate how the database can be used to calibrate constitutive models used in nonlinear finite element analysis. **DOI: 10.1061/JSENDH.STENG-12037.** © 2023 American Society of Civil Engineers.

Author keywords: Structural steel; Plasticity; Cyclic loading; Finite element analysis; Shape memory alloys; High performance steel.

Introduction

Computational models of varying fidelities are required to predict the performance of structures subjected to natural hazards (Deierlein and Zsarnóczay 2019). For instance, both fiber-based and continuum finite elements are frequently used in earthquake engineering applications. These types of elements require a mathematical representation of the material's stress-strain behavior, which is usually accomplished through phenomenological constitutive models, e.g., Voce (1948), Kent and Park (1971), Dafalias and Popov (1975), Chaboche et al. (1979), Filippou et al. (1983), Chang and Mander (1994), Hajjar et al. (1998), and Hartloper et al. (2021). Phenomenological constitutive models have one or more parameters that

¹Visiting Researcher, Dept. of Civil and Environmental Engineering, Imperial College London, Skempton Bldg. Room 412, London SW7 2BU, UK (corresponding author). ORCID: https://orcid.org/0000-0003 -3120-1748. Email: a.hartloper@imperial.ac.uk

²Doctoral Assistant, School of Architecture, Civil, and Environmental Engineering, École Polytechnique Fédérale de Lausanne, Resilient Steel Structures Laboratory, GC B3 465 Station 18, Lausanne 1015, Switzerland. Email: selimcan.ozden@epfl.ch

³Postdoctoral Researcher, School of Architecture, Civil, and Environmental Engineering, École Polytechnique Fédérale de Lausanne, Resilient Steel Structures Laboratory, GC B3 465, Station 18, Lausanne 1015, Switzerland. Email: albano.sousa@epfl.ch

⁴Associate Professor, School of Architecture, Civil, and Environmental Engineering, École Polytechnique Fédérale de Lausanne, Resilient Steel Structures Laboratory, GC B3 485, Station 18, Lausanne 1015, Switzerland. ORCID: https://orcid.org/0000-0003-0682-4660. Email: dimitrios.lignos@epfl.ch

Note. This manuscript was submitted on September 1, 2022; approved on December 26, 2022; published online on February 26, 2023. Discussion period open until July 26, 2023; separate discussions must be submitted for individual papers. This paper is part of the *Journal of Structural Engineering*, © ASCE, ISSN 0733-9445.

need to be defined; these parameters are typically defined using experiments conducted at the material scale. Therefore, databases of experiments on structural materials are a valuable tool for the reliable modeling of structural components.

In the context of earthquake engineering, structural components in steel buildings subjected to earthquake loading may experience inelastic cyclic straining. Earthquakes are erratic; therefore, the precise strain history in any component is not known in advance. It is challenging to calibrate constitutive model parameters in this context because the outcome depends on the stress-strain input used for calibration (Cooke and Kanvinde 2015; de Castro e Sousa et al. 2020). One method of addressing this challenge is to use data that is deemed to be representative of the stress-strain history expected in components subjected to earthquake loading (de Castro e Sousa et al. 2020). This approach advocates the use of uniaxial tests on multiple specimens obtained from the same material source, where each specimen is subjected to a different representative strain-based load protocol. Descriptions of the load protocols can be found in de Castro e Sousa et al. (2020). Constitutive model parameters calibrated using this representative data tend to provide a consistent prediction of the material behavior under inelastic cyclic straining, regardless of the strain history.

The aim of this paper is to establish a database of material-scale uniaxial experiments, primarily conducted at EPFL, to assist with simulating the monotonic and cyclic behavior of structural steel materials and components. This database is continuously expanding. The database primarily consists of stress-strain data from test specimens subjected to cyclic loading consistent with earthquake-induced demands. Although the data can be used in general for modeling structural steels subjected to nominally varying strain amplitudes up to around 5%, it is expected to be of primary interest to those working in earthquake engineering. Furthermore, the database can be used to evaluate macroscopic mechanical properties, such as cyclic hardening, strain rate effects, discontinuous yielding

in mild steels, and others as needs evolve in the future. In this paper, the database will first be introduced; second, the experimental and post-processing methodologies will be described; third, representative samples will be used to validate the data; and fourth, examples will demonstrate the utility of the database.

Database Summary

The database of uniaxial tests established in this paper is available for public use via Hartloper et al. (2022). Table 1 outlines the experiments contained in the database in terms of the materials, measured initial yield properties (defined later) and the number of tests in a dataset corresponding to each source. This table is ordered first by date of publication, then alphabetically within the same year. This data is from two pools: (1) data from experiments that were

conducted before the methodology in this paper was established (Grigoriou and Lignos 2017; Suzuki and Lignos 2021); and (2) data from experiments conducted according to the procedures outlined later in the Methodology section of this paper (Garcia 2020; Heredia Rosa et al. 2021; Hartloper et al. 2021; Ozden 2021; El Jisr 2022; Inamasu et al. 2022). Table 1 also includes tests that have been conducted according to the outlined methodology as a part of an ongoing effort to characterize and model structural steel materials (denoted by the "Current" reference). The database, which is continuously evolving, currently contains 353 individual experiments on structural metallic materials.

The materials in the database are primarily structural steels, and one is an iron-based shape memory alloy (Fe-SMA) (Heredia Rosa et al. 2021). The structural steels are largely used for conventional construction and seismic applications in Europe (S355J2+M, S355J2+N, S235/275JR+AR), North America (A500 Gr. B, A992

Table 1. Summary of datasets currently in the database with measured initial yield properties used in validation

	Reference Grigoriou and Lignos (2017) ^b				f_{ym} (MPa)	E_m (GPa)		
ID		Grade	Spec.a	Source	π 358.4	CoV	$\frac{\mu}{218.5}$	CoV 8.0	$\frac{N_T}{10}$
1		S355	J2+N	25 mm plate		1.4			
2				50 mm plate	340.2	2.2	205.8	10.1	10
3		S460	NL	25 mm plate	447.4	2.8	195.0	10.2	8
4		S690	QL	25 mm plate	705.7	3.3	206.2	3.7	8
5	Garcia (2020)	S690	QL	10 mm plate	765.2	3.2	205.6	5.6	4
6				HAZ^{c}	669.0	11.7	211.0	13.9	5
7	Hartloper et al. (2021)	S355	J2+M	HEB500 flange	305.3	9.1	216.3	4.1	5
8				HEB500 web	349.9	8.1	209.7	5.3	11
9	Heredia Rosa et al. (2021)	Fe-SMA	N/A	Rebar	445.0	13.1	180.3	6.8	9
10	Ozden (2021)	S355	J2+N	15 mm plate	411.7	2.7	191.5	2.7	11
11				15 mm plate 10 C/s ^d	366.9	4.5	167.2	9.2	11
12				15 mm plate 12.5 C/s ^d	365.4	8.9	190.4	14.3	10
13	Suzuki and Lignos (2021) ^b	A500	Gr. B	HSS305X16 flat	343.4	10.2	184.3	6.2	5
14		A992	Gr. 50	W14X82 flange	393.4	9.6	206.2	5.1	5
15				W14X82 web	385.8	3.4	208.0	5.5	5
16		BCP325	N/A	22 mm plate	380.3	4.0	212.6	1.4	5
17		BCR295	N/A	HSS350X22 corner	391.5	10.2	196.3	4.5	5
18		HYP400	N/A	27 mm plate	463.2	5.4	229.7	0.5	5
19	El Jisr (2022)	S355	J2+M	HEM320 flange	392.0	10.0	199.7	4.5	12
20				HEM320 web	404.8	4.3	198.5	5.3	11
21				IPE360 flange	366.4	7.4	196.0	6.0	12
22				IPE360 web	401.3	3.6	200.8	5.1	11
23			J2+N	15 mm plate	390.3	2.3	219.0	6.9	12
24	Inamasu et al. (2022)	S355	J2+M	IPE400 flange	388.7	1.8	201.7	7.2	12
25				IPE400 web	425.5	1.7	202.1	5.5	11
26	Skiadopoulos (2022)	SM490A	N/A	HM498x432x45_70 flange	342.8	7.1	199.4	2.5	10
27	1			HM498x432x45_70 web	337.8	1.5	207.2	1.9	10
28		SN490B	N/A	HY650x300x16x25 flange	356.8	2.6	207.5	3.3	10
29				HY650x300x16x25 web	389.6	1.2	198.8	2.2	10
30	Current	S235/275	JR+AR	15 mm plate	283.5	4.2	188.0	3.0	11
31		S355	J2+M	HEA160 flange	389.9	7.1	215.6	8.5	10
32				HEM300 flange	385.7		227.4		1
33				HEM500 flange	398.2	6.6	206.7	4.6	10
34				HEM500 web	427.4	2.9	196.8	3.6	9
35				IPE200 flange	383.7	7.9	205.9	7.7	10
36				IPE270 flange	405.2	5.6	212.8	7.6	14
37				IPE330 flange	393.1	3.7	208.0	8.1	10
38				IPE330 web	401.6	1.0	217.1	5.5	10
39		S690	QL	12 mm plate	776.5	1.3	198.8	6.0	10
40			~~	20 mm plate	737.5	1.9	191.2	3.1	5

Note: μ = mean; CoV = coefficient of variation in (%); and N_T = number of tests in dataset.

^aEuropean steel specifications (CEN 2005a): J2 = minimum 27 J impact energy at -20° C; JR = minimum 27 J impact energy at $+20^{\circ}$ C; N = normalized; Q = quenched; L = low temperature; +AR = as rolled; +M = thermomechanically formed; and +N = normalized.

^bDownsampled data not available.

^cThermally processed specimens.

^dHeat affected zone of welded connection.

Table 2. Available structural steel chemical compositions from manufacturers' mill certificates (% mass) (IDs correspond to Table 1)

Grade, Spec.	IDs	C	Mn	P	S	Si	Cu	Ni	Cr	Mo	V	Nb	Al
A500, Gr. B	13	0.190	0.760	0.008	0.008	0.010	0.025	0.010	0.028	0.003	0.002	_	0.035
A992, Gr. 50	14, 15	0.070	1.100	0.012	0.023	0.310	0.280	0.110	0.080	0.030	0.000	_	_
BCP325, N/A	16	0.150	1.500	0.009	0.001	0.210	0.120	0.013	0.016	0.000	0.060	_	_
BCR295, N/A	17	0.090	1.260	0.013	0.004	0.010	_	0.010	0.020	0.000	0.001	_	_
HYP400, N/A	18	0.090	1.490	0.007	0.001	0.180	0.014	0.014	0.014	0.000	0.000	0.010	0.037
S355, J2+M	19, 20	0.090	1.380	0.018	0.021	0.240	0.230	0.140	0.100	0.040	0.041	0.008	0.011
S355, J2+M	21, 22	0.080	1.390	0.016	0.021	0.190	0.290	0.140	0.090	0.030	0.007	0.037	0.015
S355, J2+M	24, 25	0.090	1.150	0.022	0.021	0.160	0.420	0.210	0.110	0.040	0.029	0.024	0.001
S355, J2+M	31	0.070	1.210	0.022	0.021	0.160	0.370	0.170	0.120	0.030	0.003	0.035	0.002
S355, J2+M	35	0.080	1.160	0.018	0.013	0.180	0.250	0.160	0.080	0.040	0.002	0.038	0.001
S355, J2+N	1	0.159	1.550	0.014	0.001	0.496	0.015	0.039	0.048	0.020	0.001	0.000	0.049
S355, J2+N	2	0.166	1.550	0.015	0.001	0.490	0.020	0.028	0.038	0.007	0.000	0.000	0.049
S355, J2+N	10, 11, 12	0.160	1.460	0.018	0.003	0.220	0.060	0.030	0.040	0.010	0.005	0.005	0.032
S355, J2+N	23	0.160	1.550	0.010	0.002	0.190	0.060	0.050	0.040	0.002	0.003	0.001	0.042
S460, NL	3	0.180	1.540	0.012	0.001	0.260	0.010	0.470	0.030	0.000	0.074	0.033	0.034
S690, QL	4	0.086	1.650	0.009	0.001	0.393	0.020	0.180	0.176	0.215	0.035	0.026	0.088
S690, QL	39	0.143	1.233	0.011	0.001	0.362	0.006	0.059	0.252	0.131	0.037	0.003	0.033
S690, QL	40	0.161	1.120	0.007	0.000	0.290	0.012	0.050	0.200	0.084	0.030	0.001	0.091
SM490A, N/A	26, 27	0.160	1.400	0.017	0.004	0.300	_	_	_	_	_	_	_
SN490B, N/A	28, 29	0.180	1.070	0.019	0.008	0.340	_	0.010	0.050	0.010	0.000	_	0.016

Gr. 50) and Japan (BCP325, BCR295, SN490, SM490); two highstrength steels (S690QL, S460NL) and a high yield point steel (HYP400) are also included. Specifications ("Spec." column in Table 1) are provided for each dataset; see the relevant standards for details (CEN 2005a, c; JISC 2014; ASTM 2015, 2018; Suzuki et al. 2008; CEN 2019a, b). The sources for the specimens are either from standardized profiles (e.g., IPE400, W14X82, HSS305X16), or plates. Each ID in Table 1 corresponds to a different heat for specimens fabricated from plates, whereas the flange and web specimens of a particular profile are from the same heat. The test specimens were typically fabricated from the base material; however, two datasets are based on test specimens that underwent thermal processing to replicate a heat affected zone (S355J2 15 mm 10/12.5 C/s) (Ozden 2021), and one dataset is based on test specimens that were machined from the heat affected zone (HAZ) of steel tubes (S690QL HAZ) (Garcia 2020). Details regarding the fabrication procedures, resulting microstructures, and results from these experiments can be found in the cited literature. There are currently 11 steel grades from 39 sources. The available chemical compositions for structural steels have also been summarized in Table 2. This information may be of interest to examine aspects such as the weldability of the base metal, among others.

Methodology

The proposed database consists of data obtained from mechanical tests on samples of metallic materials. Fig. 1 summarizes the overall methodology used to generate this data: (1) material specimen extraction and manufacturing, (2) material testing, and (3) data post-processing. The post-processed data can then be used in applications, such as calibrating empirical constitutive models.

Material Specimen Extraction and Manufacturing

Test specimens were fabricated from sources, such as rolled steel profiles or plates (Fig. 1) manufactured according to relevant standards (ASTM 2015, 2016b, 2018; CEN 2005c; JISC 2014). The three standard specimen geometries shown in Fig. 2 were specified to accommodate a range of plate thicknesses, namely test specimens with an 8, 12, and 20 mm nominal diameter (M8, M12 and M20, respectively). Pieces roughly the size of the specimen were cut from the flange/web of a profile or plate, then the pieces were machined into the test specimens, as illustrated schematically in Fig. 1. Multiple specimens were manufactured from each source to accommodate the different load protocols described later. The reduced sections specified in Fig. 2 were designed to reduce

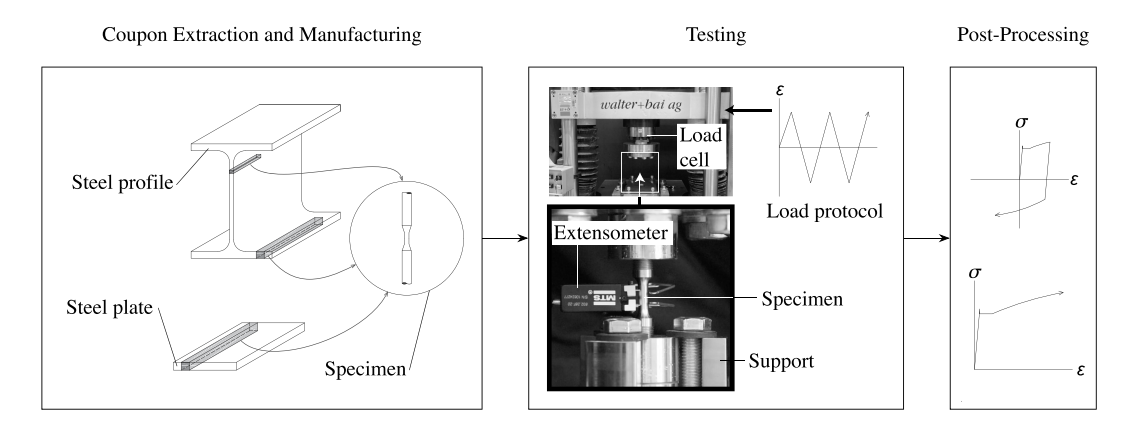


Fig. 1. Workflow for the experiments and data post-processing.

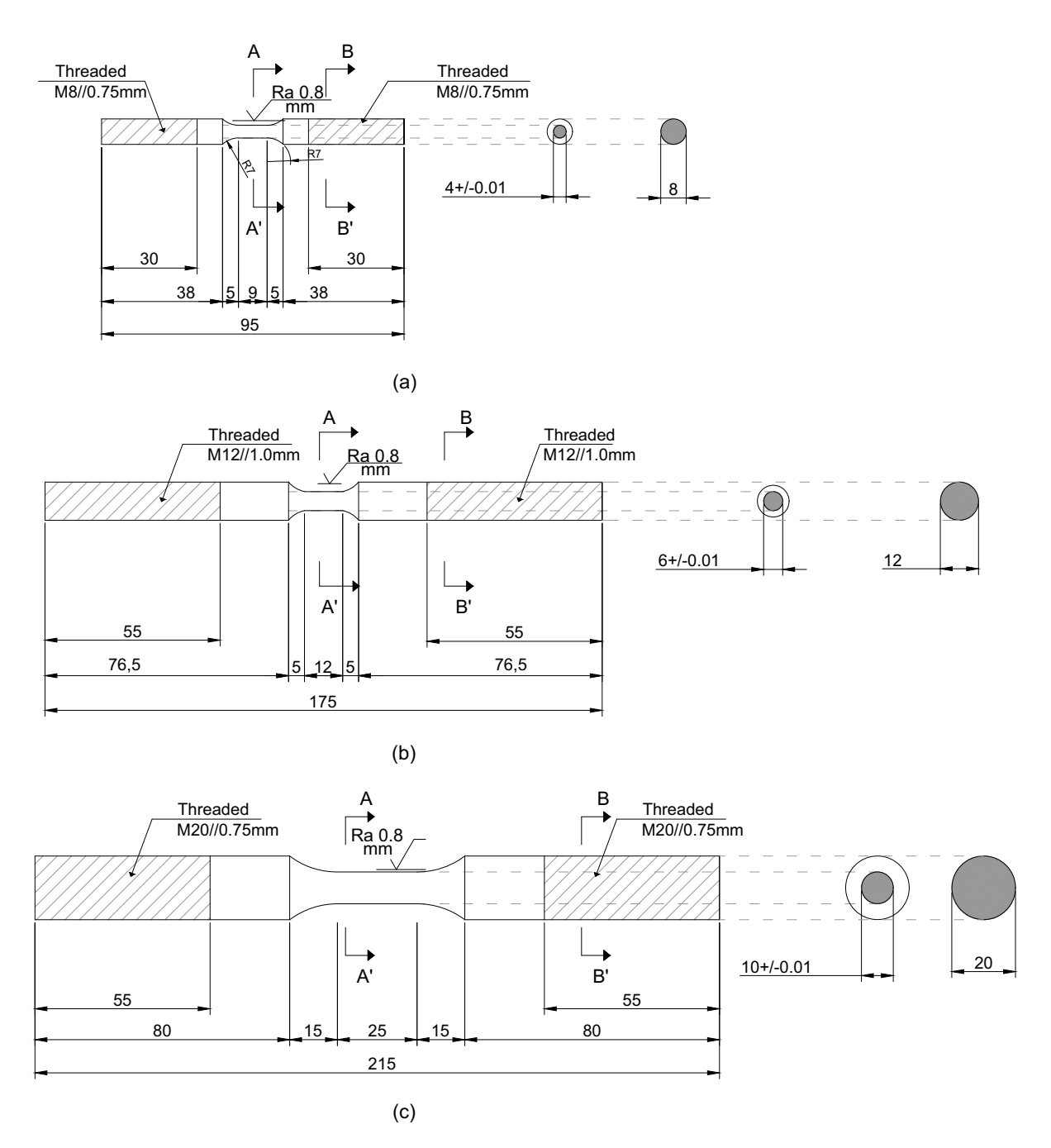


Fig. 2. Test specimen geometry: (a) M8 specimen; (b) M12 specimen; and (c) M20 specimen.

the diameters to half the nominal values with a length compatible with the extensometers used in the experiments. The compact specimen geometry was used to delay buckling of the specimens under the high compressive strains that were be applied (e.g., greater than 5% strain in compression).

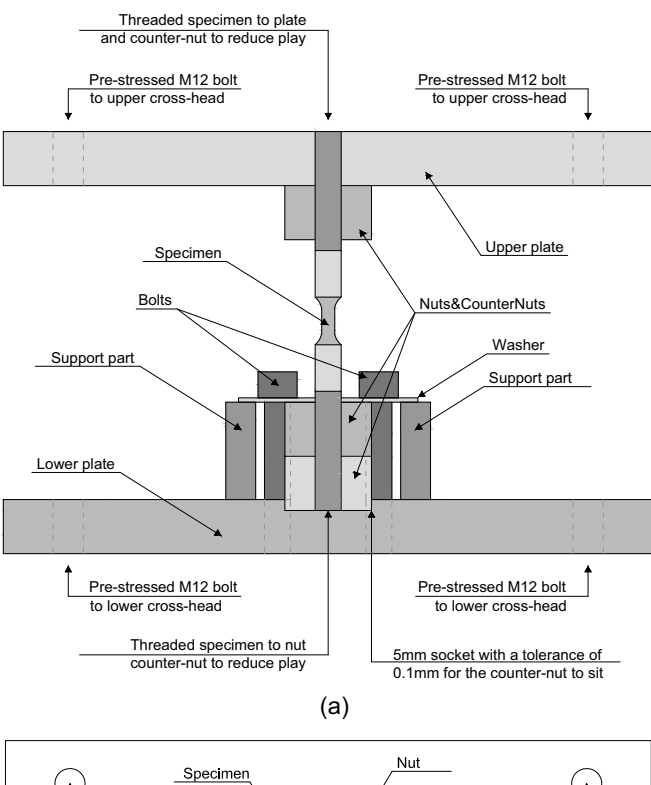
Test Setup

The walter+bai uniaxial testing machine in EPFL's structures laboratory, shown in Fig. 1, was used in a majority of the experiments in Table 1. This testing machine is verified and calibrated according to ASTM E4 (ASTM 2021) and ASTM E83 (ASTM 2016a) every two years. This setup aims to ensure the vertical alignment of the test specimen during tension-compression testing; its details are shown in Fig. 3. This test apparatus was assembled as follows: first, the upper plate shown in Fig. 3 was pre-stressed to the cross-head.

Second, the nuts and counter nuts were screwed onto the specimen and the specimen was screwed into the upper plate. Third, the 5 mm socket on the lower plate was aligned with the specimen, the support parts were prestressed to the lower plate to avoid slip, and the lower plate was prestressed to the testing machine. This process ensures vertical alignment (concentricity) of the test specimen within the fabrication tolerance of the specimen itself. Fourth, bolts were pretensioned atop the supports on the lower plate to allow for the application of tension to the test specimen. Loading was then applied through an electric motor that drives the testing machine's cross-head.

Instrumentation and Data Acquisition

Strain measurements were recorded using an MTS extensometer with a gauge length of 8 mm for the M8 and M12 specimens (Fig. 1), and with a gauge length of 20 mm for the M20 specimens.



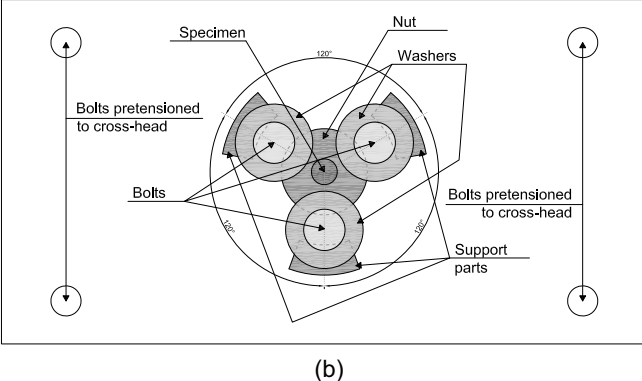


Fig. 3. Details of the test setup for the M12 test specimen: (a) cross section; and (b) plan view. (Reprinted from Construction and Building Materials, Vol. 272, Diego Isidoro Heredia Rosa, Alexander Hartloper, Albano deCastro e Sousa, Dimitrios G. Lignos, Masoud Motavalli, Elyas Ghafoori, "Experimental behavior of iron-based shape memory alloys under cyclic loading histories," pp. 121712, © 2021, with permission from Elsevier.)

Both extensometers meet or exceed the requirements for calibration according to the ASTM E83 Class B1 (ASTM 2016a) standard. These extensometers employed up to 12.5% strain due to their maximum allowable displacement. The force was measured through a load cell fixed to the cross-head of the testing machine (Fig. 1). The surface temperature of the test specimen was measured in selected cases using a PT100 temperature sensor attached to the reduced section (Heredia Rosa et al. 2021). A video extensometer using target recognition was used for the strain measurements in Grigoriou and Lignos (2017).

A metadata file was recorded with each test that included: material source of the test specimen, nominal material properties, load protocol tested, measured geometric properties, date of the test, and other pertinent information. The chemical composition was recorded using the mill certificate provided by the fabricator, when available. Raw data collected during the experiments included:

time, cross-head displacement, load cell force, extensometer displacement, surface temperature (when available), and video footage (when available). The cross-head displacement, extensometer displacement, and load cell force were sampled at a frequency of 20 Hz. This raw data was then post-processed as discussed in a following section.

Loading Protocols and Test Methodology

Each test consisted of a sequence of target strains applied to the test specimen at specific strain rates. The target strains were defined by load protocols (LPs) schematically summarized in Fig. 4. Each specimen was subjected to a single load protocol (i.e., multiple specimens were required for multiple load protocols). The LPs, and their relation to strain demands expected in components subjected to earthquake loading, were described in detail in de Castro e Sousa et al. (2020) and Heredia Rosa et al. (2021). Briefly, they include: tensile loading until fracture (LP1), one cycle followed by tensile loading until fracture (LPs 2 and 3), constant amplitude loading (LPs 4 and 5), increasing amplitude cyclic loading (LPs 6–8), random cyclic loading (LP9), and cyclic loading with an increasing tensile mean offset until fracture (LP10).

The initial loading sequence was operated in load control up to $0.65f_{yn}$, where f_{yn} is the nominal yield stress of the material being tested. Tests were then operated in closed-loop strain control based on the guidelines for uniaxial testing in ASTM E8/E8M (ASTM 2016c). A strain rate of 0.0003 mm/mm/s prior to 2% strain amplitude was employed based on the upper bound specified in ASTM E8/E8M for determining yield properties. Once past 2% strain in absolute value, the strain rate was increased to 0.008 mm/mm/s based on the upper bound in ASTM E8/E8M for determining ultimate properties. Cross-head displacement control was used after 12.5% strain for the LPs that specified loading until fracture (LPs 1, 2, 3, 10), due to the extensometer limit noted earlier. Control in each experiment was established using the standard form of the proportional-integral-derivative (PID) algorithm with a walter+bail PCS8000 controller and the software DION7 version 2.1.0.

The use of closed-loop strain control allows for greater control over the strain rate; however, the overall stability of the test is a concern (ASTM 2016c). Stability of the test is a key concern during inelastic loading because the tangent modulus decreases as loading increases; therefore, the unit change in control variable required to induce a unit change in strain also decreases. Incorrect PID parameters lead to oscillations in the stress-strain response, particularly within the yield plateau and as the tangent modulus approaches zero prior to necking of the specimen. To alleviate this issue, the PID control parameters for a particular material and geometry were determined through a trial test that included inelastic cycles; these parameters were then used for the remaining LPs. Alternatively, the proportional constant calibrated to the elastic response can be multiplied by a factor of around 1/3-1/5 to improve control during inelastic loading. The derivative component of the PID algorithm is neglected in all cases.

Data Post-Processing: Deduced Quantities

Post-processing is required to deduce the required data from the raw measurements. The engineering and true stress/strain, and the estimated fracture strain when applicable, are all included in the proposed database. The engineering strain, ε_{enq} , is

$$\varepsilon_{eng} = \delta_{extenso} / L_{extenso} \tag{1}$$

where $\delta_{extenso}$ is the extensometer displacement; and $L_{extenso}$ is the extensometer gauge length. The true strain, ε , is

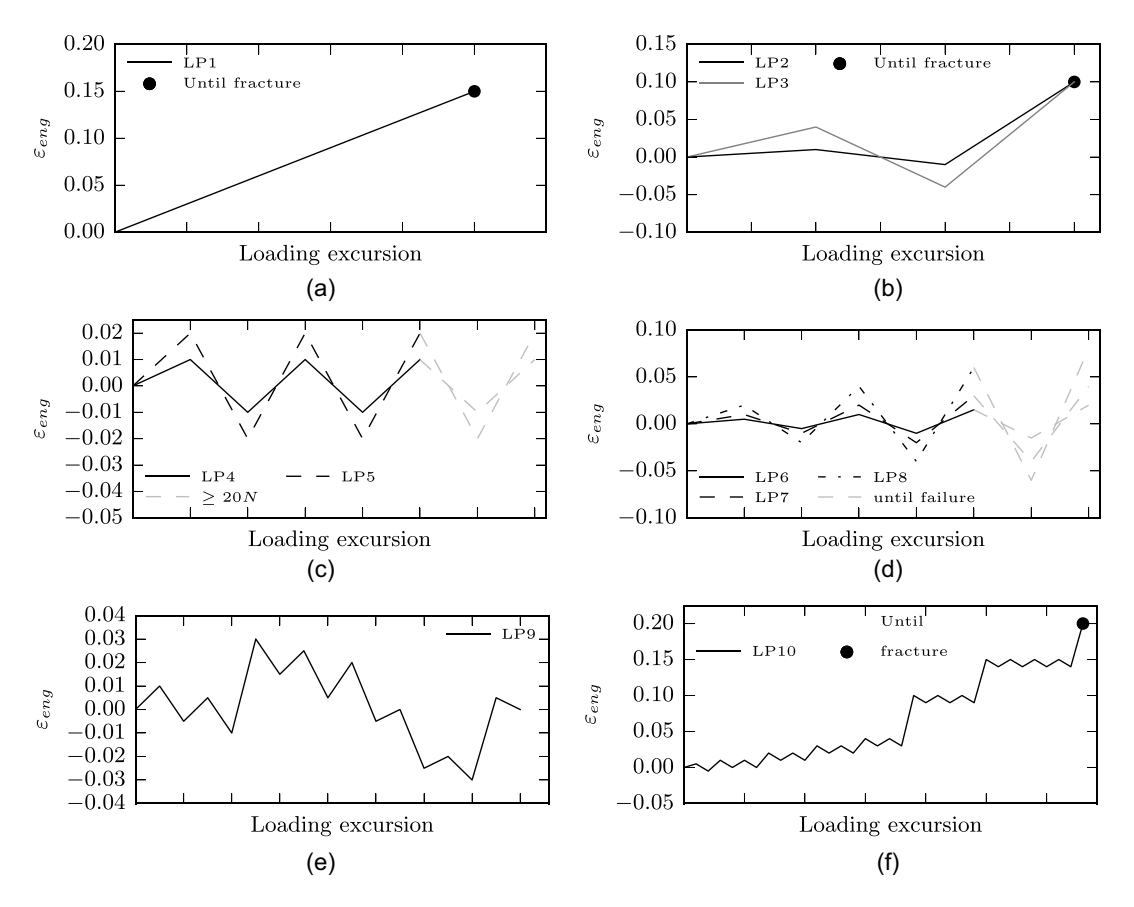


Fig. 4. Load protocols used in the experiments; loading excursion axis is schematic: (a) LP1: monotonic tensile test; (b) LPs 2 and 3: one cycle each at 1% and 4% to fracture, respectively; (c) LPs 4 and 5: constant amplitude in ranges of 2% and 4% with zero mean strain, respectively; (d) LPs 6–8: incrementally increasing ranges of 0.5%, 1%, and 2%, respectively, until specimen failure; (e) LP9: variable amplitude; and (f) LP10: asymmetric. (Reprinted from de Castro e Sousa et al. 2020, ©ASCE.)

$$\varepsilon = \ln[1 + \varepsilon_{eng}] \tag{2}$$

The engineering stress, σ_{eng} , is

$$\sigma_{eng} = F/A_0 \tag{3}$$

where F is the load cell force; and A_0 is the initial measured area. The measured area is computed based on the average initial diameter, D_0 , where the average initial diameter is computed as the average of three measurements of the reduced parallel section made using calipers prior to testing. The true stress, σ is

$$\sigma = \sigma_{eng}(1 + \varepsilon_{eng}) \tag{4}$$

The true strain rate, $\dot{\varepsilon}$, can then be computed using finite differences as

$$\dot{\varepsilon} = \Delta \varepsilon / \Delta t \tag{5}$$

where $\Delta \varepsilon$ is the difference in true strain between time points; and Δt is the time step.

For loading protocols specifying tensile loading until facture (LPs 1, 2, 3, 10), the true stress-strain data is included up until the earlier of the extensometer limit of 12.5% strain or the maximum true stress. The average true strain across the necked specimen, ε_{frac} , is computed for these LPs as

$$\varepsilon_{frac} = 2\ln[D_0/D_{frac}] \tag{6}$$

where D_{frac} is the average diameter of the cross section measured at the fracture location using calipers. The value of D_{frac} is the average

of three measurements from the top surface and three from the bottom surface (six total). For loading protocols that specify increasing compressive strains (LPs 6, 7, 8) the true-stress strain data is included up to the initiation of buckling. This point may be specified using visual data if it is available (e.g., from video recordings); otherwise, the data is truncated at the point of unloading after the first excursion past 5% strain in tension.

The initial elastic modulus and initial yield stress are also deduced from the true stress-strain data as a part of validating the results. Although the primary intent of our database is to provide stress-strain data on the inelastic cyclic behavior of structural metallic materials, the initial elastic modulus and yield stress are useful parameters because they can be easily compared with existing results. We emphasize that the initial elastic modulus and yield stress may not be strictly determined according to standards such as ASTM E111 (ASTM 2017), because the focus of the experiments was to obtain the cyclic response defined by the load protocols outlined in the Load Protocols and Test Methodology section. The measured initial elastic modulus, E_m , is computed using a linear regression fit to the initial data points between $[0.01f_{vn}, 0.66f_{vn}]$. The lower bound of $0.01f_{yn}$ is specified to avoid noise in the measurements at very low stresses and the upper bound is specified to ensure elastic behavior. The initial elastic modulus is then used to compute the measured initial yield stress, f_{vm} , using the 0.2% offset method (ASTM 2016c). The initial yield properties are discarded if E_m differs by more than 25% from its nominal value of $E_n = 200$ GPa. This criterion indicates that there was low quality data in the elastic region and/or there were errors in the test

specimen manufacturing (e.g., significant out-of-straightness in the specimen).

Data Post-Processing: Downsampling the Stress-Strain Data

A large volume of data points (e.g., tens to hundreds of thousands) are generated for each test using the proposed strain rates with the data acquisition sampling rate of 20 Hz. The number of data points becomes an issue for constitutive model calibration because the time required to run the calibration is directly related to the number of data points in each test. The calibration time becomes especially burdensome for optimization algorithms that compute gradients and Hessians, such as those used in de Castro e Sousa et al. (2020) and Hartloper et al. (2021).

A downsampling strategy is proposed to address this issue by reducing the number of data points. The first step of the strategy is to identify and sample the points of load reversal (i.e., the peaks in the stress-strain graph). This step provides a set of sample points k_1 . The second step is to use the Ramer-Douglas-Peucker (Ramer 1972; Douglas and Peucker 1973) line simplification algorithm (RDP algorithm) to reduce the number of data points but retain the curvature in the stress-strain graph. Very briefly, the RDP algorithm approximates the least number of samples such that perpendicular distance between all the sampled points is less than a predefined tolerance (ϵ) . The second step provides a set of sample points k_2 . The third step is to sample a few additional points in the initial elastic region, as defined up to $0.8f_{vn}$, to ensure accuracy when computing the initial elastic modulus using the downsampled data. The set of sample points resulting from the third step is k_3 . Then the final set of sampled points is the union of k_1 , k_2 , and k_3 to combine the results of the three steps.

Some processing is required to improve the results from the RDP algorithm in the second step. First, the stress signal is filtered using a moving average filter to reduce potential oscillations in the stress signal resulting from the closed loop strain control. The filtering is important to sample points based on the steady-state response rather than the oscillating signal. Second, the stress and strain signals are normalized by their ranges (i.e., $\sigma^* = \sigma/(\max \sigma - \min \sigma)$) to handle the difference in units between these quantities. This normalization is important, as the RDP algorithm computes perpendicular distances using the 2-norm. The filtered, normalized data is only used by the RDP algorithm to determine the sample points in the original data, i.e., the final output is a subset of the original data and is neither filtered nor normalized. Finally, the tolerance parameter in the RDP algorithm, ϵ , is selected such that the overall difference in the strain energy between the original and downsampled data is less than 0.5%. The entire downsampling method has been implemented in the post-processing library rlmtp (Hartloper 2022), examples will be shown later in the Results section.

Results

Available Data

The open-access database (Hartloper et al. 2022) is summarized in Table 1. The experiments from Grigoriou and Lignos (2017) and Suzuki and Lignos (2021) (70 total) only include the true stress-strain and they have not been downsampled. All the other experiments in Table 1 were conducted and processed using the load protocols and methodology outlined in this paper. Note that temperature data is only available for the Fe-SMA. Finally, not all load protocols were conducted for each source and some load

protocols may have been repeated to establish consistency or due to errors in prior experiments.

Data Verification

The average initial yield properties are computed and included in Table 1 for each dataset to verify the integrity of the data. Specifically, the average measured initial yield stress and average initial elastic modulus are provided for all the datasets. Note that 12 experiments are excluded because they have E_m with greater than 25% variance from the nominal value of 200 GPa (five exclusions are associated with manufacturing errors and seven are associated with low quality data). Using the S355 steels as an example, there are a total of 202 experiments from 20 datasets (heat treated materials are excluded). The initial yield stress for each dataset is within the range of 305-430 MPa; the initial yield stress was below the nominal value of 355 MPa for this material in only three datasets. The average f_{ym} across the 20 datasets is 386 MPa with a coefficient of variation (CoV, CoV = mean/standard deviation) within 1% to 10% across all the datasets. This mean value is 9% higher than the nominal value of 355 MPa, but somewhat lower than the average of 406 MPa with a CoV of 17% found in Sadowski et al. (2015) based on 31 observations of S355J2+N steel. The average initial elastic modulus across all S355 datasets is $E_m = 208$ GPa, which is near the nominal value of 210 GPa (CEN 2005b) and agrees with that found by Sadowski et al. (2015). The initial elastic modulus of S355 steel is within 190-230 GPa, with a CoV between 3% and 10% within each dataset. These CoV values are deemed to be reasonably consistent with the average of 6% to 7% for various S355 steel plates reported in Braconi et al. (2013) and the 13% for various European structural steels reported in Sadowski et al. (2015).

The efficiency of the downsampling method is computed through the reduction factor N_{orig}/N_{ds} , where N_{orig} is the number of points in the original data and N_{ds} is the number of points in the downsampled data. The average reduction in data points is $N_{orig}/N_{ds}=89$ across the 277 experiments that were considered. A specific example is shown in Fig. 5 for LPs 1 and 8 of the S355J2+M HEM320 web dataset. The downsampler reduces the number of data points by 323 times for LP 1 and 97 times for LP 8 in these specific cases. Note that the downsampling method is efficient because it samples more points in the regions of higher curvature to keep the fidelity of the stress-strain results. With regards to the initial yield properties, the average relative difference in the elastic modulus, E_m , between the original and downsampled data is 1.9% and the average relative difference in the yield stress, f_{vm} , is 0.13%.

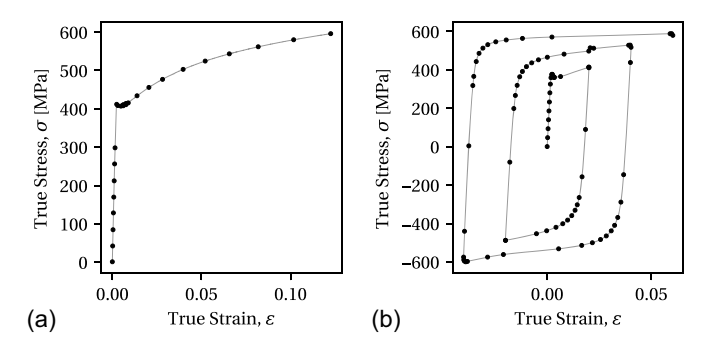


Fig. 5. Original data (line) and sampled points (dots) from the S355J2 +M HEB320 web dataset: (a) LP1: $N_{orig} = 8715$, $N_{ds} = 27$; and (b) LP8: $N_{orig} = 7916$, $N_{ds} = 82$. N_{orig} is the number of points prior to downsampling; and N_{ds} is the number of sampled points.

Therefore, the downsampling method is reasonably effective at preserving the elastic modulus and extremely effective at preserving the initial yield stress.

The (downsampled) true stress-strain graphs for all the load protocols in the S355J2+M HEM320 web dataset are shown in Fig. 6 to illustrate typical results. The effects of discontinuous yielding (e.g., upper yield point and plateau) can be seen in these figures, along with cyclic hardening, hardening with increasing strain

amplitude, and the Bauschinger effect. The strain rates computed for LPs 3 and 8 are shown in Fig. 7. The strain rate plots show that the closed-loop test method provides reasonably good control at the target strain rate, although there is an initial overshoot in the strain rate upon each load reversal. Finally, Fig. 8 was extracted from video recordings of LP8 from the S355J2+M HEB500 web dataset to illustrate the side-sway buckling behavior typically observed at high compressive strains.

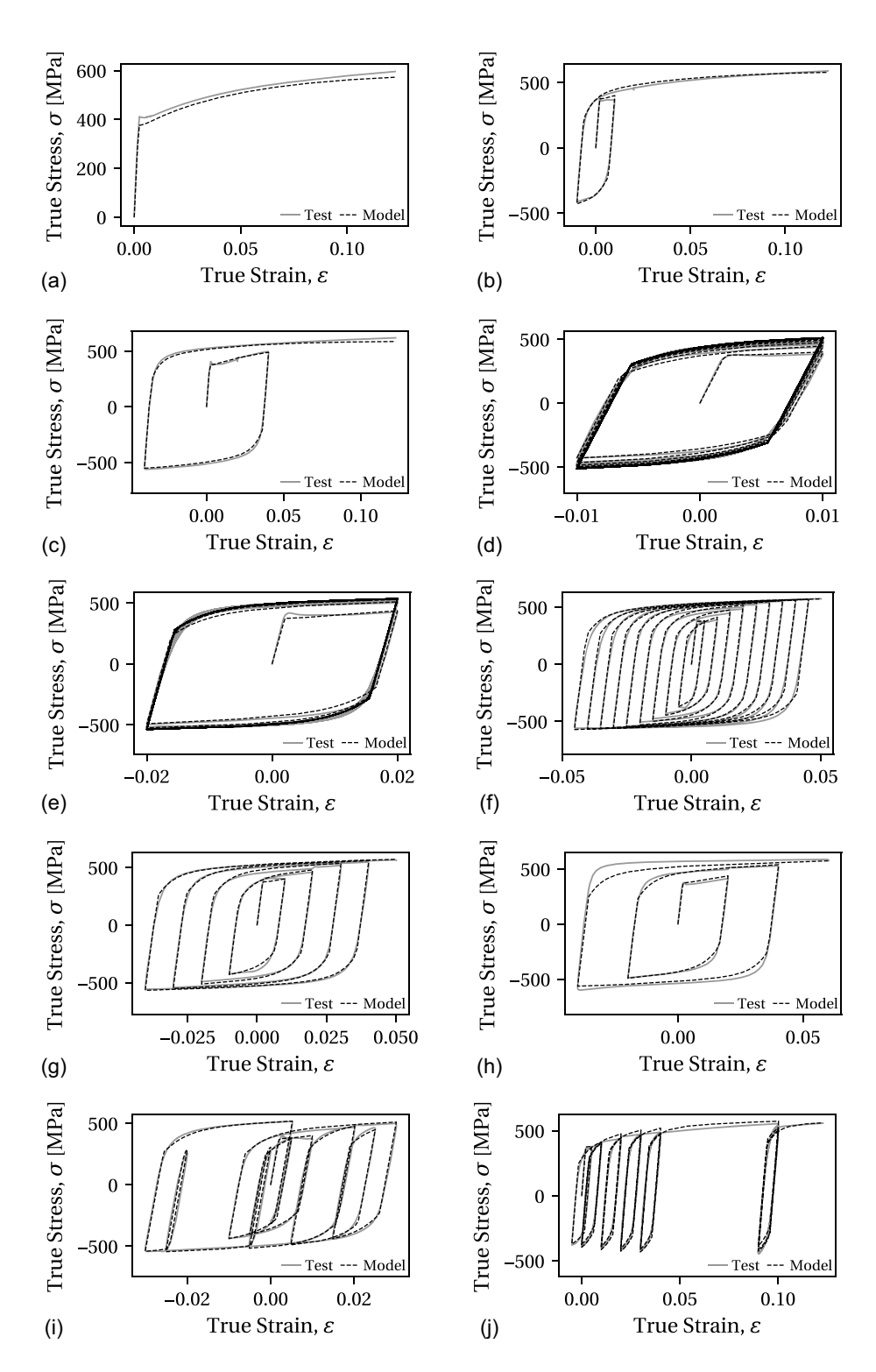


Fig. 6. S355J2+M HEM320 web dataset and UVC model prediction: (a) LP1; (b) LP2; (c) LP3; (d) LP4; (e) LP5; (f) LP6; (g) LP7; (h) LP8; (i) LP9; and (j) LP10.

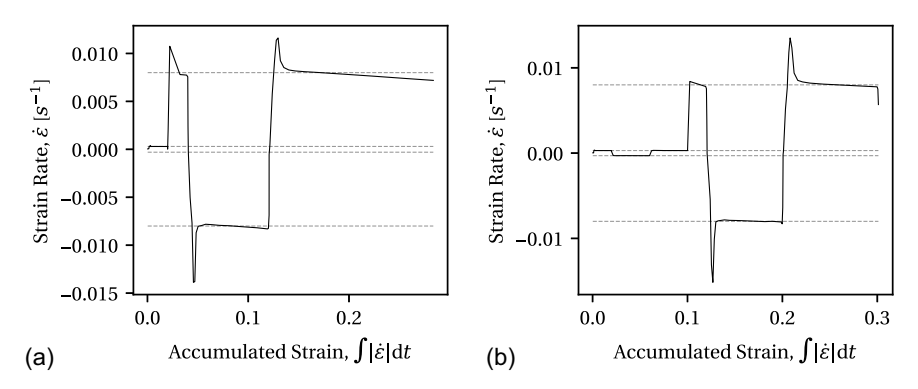
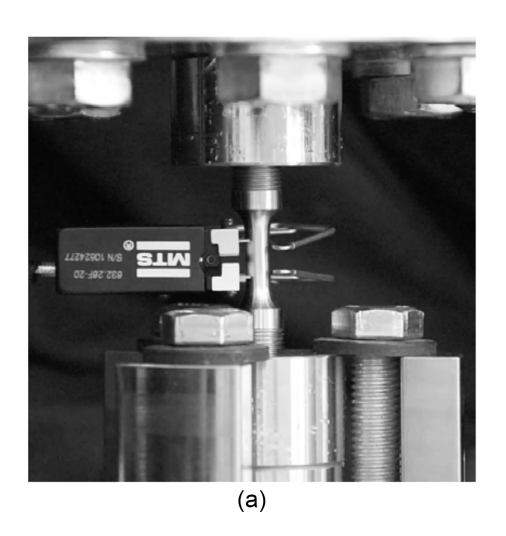


Fig. 7. Strain rates from the S355J2+M HEM320 web dataset. Dashed lines indicate the target strain rates: (a) LP 3; and (b) LP 8.



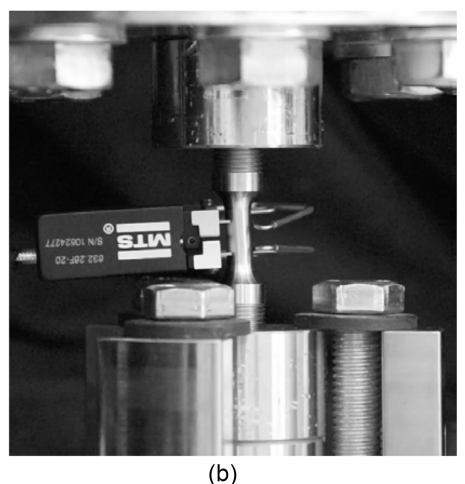


Fig. 8. S355J2+M HEB500 web, LP8 specimen at (a) 6% strain; and (b) -6% strain (side-sway buckling apparent).

Example Application: Calibrating Constitutive Model Parameters for Structural Steels

Application Methodology

The procedure for calibrating constitutive model parameters can be defined as a constrained minimization problem:

subject to
$$g(x) \le 0$$
 (7b)

where x is the vector of n constitutive model parameters; $f(x):\mathbb{R}^n \to \mathbb{R}$ is the objective function; and $g(x):\mathbb{R}^n \to \mathbb{R}^m$ is a possible vector valued function of m constraints. Suitable objective functions, constraints, and solution methods for Eqs. (7a) and (7b) have already been proposed (Cooke and Kanvinde 2015; de Castro e Sousa et al. 2020; Hartloper et al. 2021).

One suitable objective function is the sum of the difference in squared strain energy between a set of tests and the model prediction (de Castro e Sousa et al. 2020; Hartloper et al. 2021). This objective function is defined as

$$f(\mathbf{x}) = \sum_{j=1}^{N_T} \frac{\int_0^{\varepsilon_j^*} (\sigma_j^{model}(\varepsilon_j; \mathbf{x}) - \sigma_j^{test})^2 d\epsilon^*}{\int_0^{\varepsilon_j^*} d\epsilon^*}$$
(8)

where N_T load histories are considered $(j = 1, 2, ..., N_T)$; $\sigma_i^{model}(\varepsilon_i; \mathbf{x})$ is the stress from the constitutive model given strain

history ε_j and parameters x; σ_j^{test} is the stress recorded in the uniaxial test j; and ε^* is the accumulated strain, defined as

$$\varepsilon_j^* = \int_0^{t_j} \dot{\varepsilon}_j \mathrm{d}\tau \tag{9}$$

We note the importance of defining the objective function in Eq. (8) as an integral when downsampled data is used. This is because the integral form is less sensitive to the density of data points than, for example, a least-squares approach.

Stress-strain data is necessary to define ε_j and σ_j^{test} in Eq. (8). The objective function also requires the inclusion of N_T different tests to obtain consistent simulations by combining the results from different load protocols from a particular source (de Castro e Sousa et al. 2020). Rate-dependent and temperature-dependent constitutive models would also require strain-rate and temperature parameters. Therefore, it is clear that the data included in the proposed database is suited to calibrating constitutive models that simulate inelastic cyclic straining.

Two datasets from the database will be used to calibrate an Updated Voce-Chaboche (UVC) constitutive model (Hartloper et al. 2021) using the algorithms provided in the publicly available Python package RESSPyLab (de Castro e Sousa et al. 2019). The UVC model was selected for this example because it demonstrates superior accuracy compared to the Voce-Chaboche model (Voce 1948; Chaboche et al. 1979), for a consistent set of model parameters regardless of the loading history and material grade (Hartloper et al. 2021). The UVC model parameters to be calibrated are

 $x = [E, \sigma_{y,0}, Q_{\infty}, b, D_{\infty}, a, C_1, \gamma_1, C_2, \gamma_2]$, where E is the elastic modulus; $\sigma_{y,0}$ is the initial yield stress; Q_{∞} is the isotropic hardening magnitude; b is the rate term associated with Q_{∞} ; D_{∞} is the isotropic hardening magnitude of yield surface reduction; a is the rate term associated with D_{∞} ; C_k are the kinematic hardening magnitudes; and γ_k are the rate terms associated with C_k (two kinematic hardening terms are considered in this paper). The calibration methodology for the UVC model, including the constraints g(x) in Eq. (7b), is defined in Hartloper et al. (2021). Finally, we emphasize that the proposed database can be used to calibrate any other

constitutive model that relies on the data contained within (e.g., uniaxial stress/strain, strain rate, temperature), and is not restricted to the UVC model.

Application Results

The S355J2+M HEM320 web and S690QL 12 mm plate datasets are used to illustrate the UVC model calibration process. The values of ε_j and σ_j^{test} in Eq. (9) are defined by the test data displayed in Fig. 6 (S355J2+M HEM320 web) and Fig. 9 (S690QL 12 mm

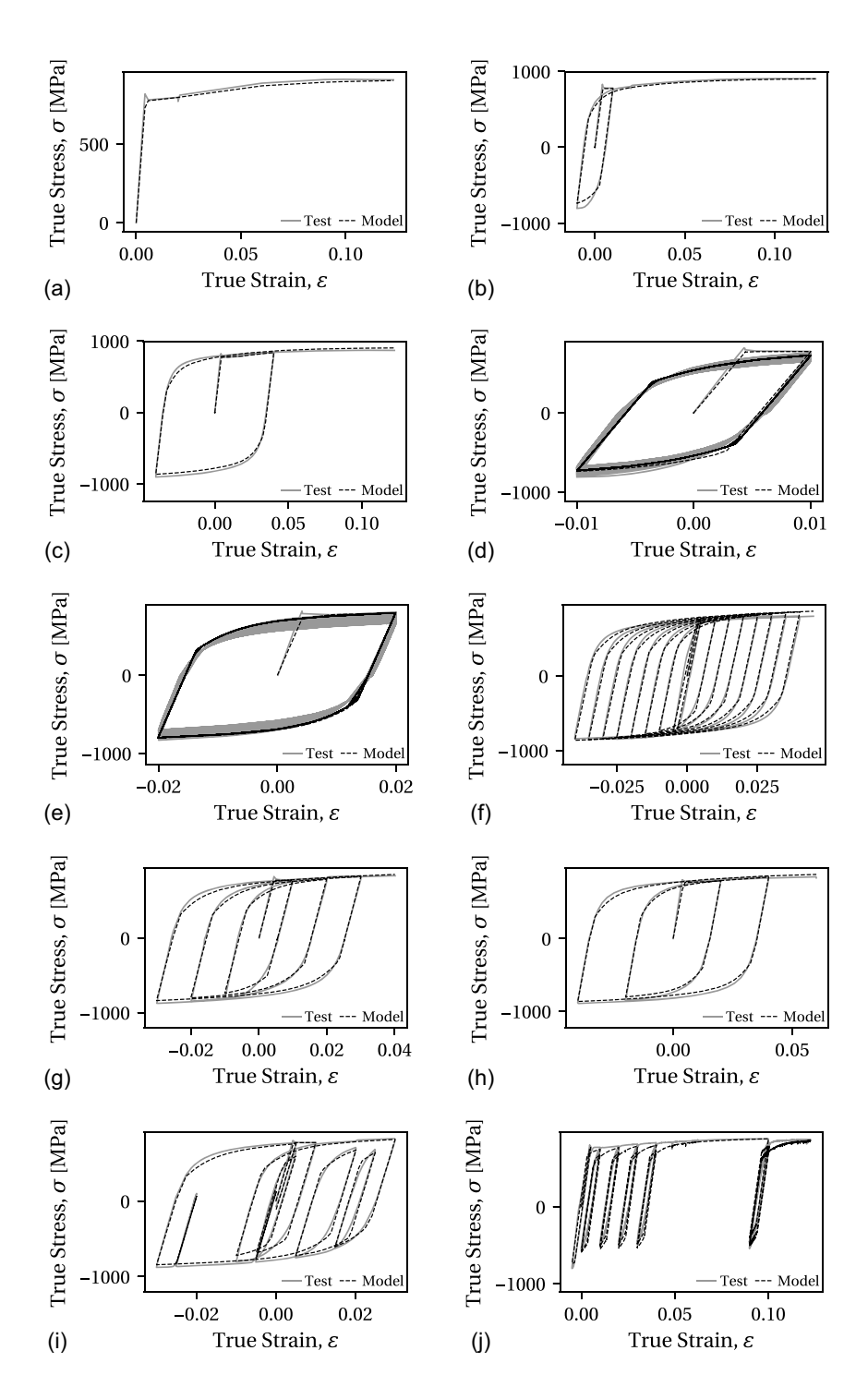


Fig. 9. S690QL 12 mm plate dataset and UVC model prediction: (a) LP1; (b) LP2; (c) LP3; (d) LP4; (e) LP5; (f) LP6; (g) LP7; (h) LP8; (i) LP9; and (j) LP10.

Table 3. UVC model parameters for selected datasets

Dataset	E (GPa)	$\sigma_{y,0}$ (MPa)	Q_{∞} (MPa)	b	D_{∞} (MPa)	а	C_1 (MPa)	γ_1	C_2 (MPa)	γ_2
S355J2+M HEB320 web S690QL 12 mm plate	184 174	376 774	133	19	99 214	255 186	20,688 34,892	218 209	2,034 4,954	23
S090QL 12 mm plate	1/4	//4	U	U	214	180	34,892	209	4,934	

plate). Parameters for the UVC model obtained using RESSPyLab are recorded in Table 3.

For the HEM320 web dataset, there is a relative error of 7% between the mean measured initial yield stress, f_{ym} , from Table 1 and the calibrated initial yield stress, $\sigma_{y,0}$. There is also a 7% relative error between the mean measured initial elastic modulus, E_m , and the calibrated elastic modulus, E. Furthermore, there is an average relative error of 5% in strain energy between the model prediction and tests for the entire dataset. This level of relative error is similar to those found for other structural steels (Hartloper et al. 2021). Overall agreement between UVC model prediction and test data is apparent in Fig. 6, as the model approximates cyclic hardening through the isotropic hardening component (Q_{∞}, b) , as well as work hardening and the Bauschinger effect through the kinematic hardening component (C_k, γ_k) .

Meanwhile, for the S690QL 12 mm plate dataset, there is a relative error of less than 1% for f_{ym} and 13% for E_m between the UVC model and test data. The parameters Q_{∞} and b are zero in Table 3 because S690QL steels do not exhibit appreciable cyclic hardening, although they still exhibit work hardening (de Castro e Sousa et al. 2020; Hartloper et al. 2021). Conversely, LPs 4 and 5 [Figs. 9(d and e)] indicate that cyclic softening occurs in this material under constant amplitude loading. This phenomenon is not fully captured by the UVC model because $Q_{\infty} > 0$ is enforced in the calibration methodology (Hartloper et al. 2021). Regardless, there is an average relative error of 7% in strain energy between the UVC model and test data of the S690QL 12 mm plate dataset; again, there is reasonably good agreement between the model and test data shown in Fig. 9.

Conclusions

The aim of this data paper was to establish a database of material-scale uniaxial experiments, primarily conducted at EPFL, to assist with simulating the monotonic and cyclic behavior of structural steel materials and components. A database of 353 uniaxial tests on structural steels was created to accomplish this objective, consisting of materials from Europe, North America, and Japan, as well as an iron-based shape memory alloy. The database assembled in this paper is a first effort at the systematic documentation of material data and will continually evolve as additional tests are conducted. The database primarily consists of stress-strain data obtained from cyclic load protocols that are deemed to be representative of the demands on steel components expected during earthquakes (de Castro e Sousa et al. 2020). All of the data is available at Hartloper et al. (2022) and the methods used to process the data are available through (Hartloper 2022).

A downsampling method was developed in this paper to support computationally efficient calibrations of constitutive models. The downsampling method reduces the number of data points by an average of 89 times while the overall difference in strain energy between the downsampled and original data is less than 0.5%. The differences in measured initial elastic modulus and yield stress between the downsampled and original data are 1.9% and 0.13%, respectively. Finally, the database established in this paper will be useful for simulating the inelastic cyclic behavior of structural

steels subjected to nominal varying strain amplitudes up to around 5%. Further uses for the database include, but are not limited to, the following. First, models other than the one shown in this paper can be calibrated and assessed using our database. Second, the data can be used to investigate the macroscopic behavior of structural metallic materials; for instance, to examine the behavior of high-strength steels, and the influence of yield point phenomena and strain-rate effects in steels. Third, the data can be used to assist in developing broad recommendations for modeling structural steels subjected to inelastic cyclic straining, similar to what has been done for tensile loading in, e.g., Braconi et al. (2013).

Data Availability Statement

Some or all data, models, or code generated or used during the study are available in a repository or online in accordance with funder data retention policies. de Castro e Sousa et al. (2019) (https://github.com/AlbanoCastroSousa/RESSPyLab), Hartloper (2022) (https://github.com/ahartloper/rlmtp), Hartloper et al. (2022) (https://doi.org/10.5281/zenodo.6965147).

Acknowledgments

This study is based on work supported by an EPFL internal grant and by the Swiss National Science Foundation (Project No. 200021_188476 and Postdoc.Mobility Grant No. 206929). The financial support is gratefully acknowledged. The authors thank Gilles Guinet for their assistance in conducting experiments at the EPFL structures laboratory. Any opinions, findings, and conclusions or recommendations expressed in this paper are those of the authors and do not necessarily reflect the view of sponsors.

Notation

The following symbols are used in this paper:

 A_0 = area of the specimen's reduced cross section prior to loading;

CoV = coefficient of variation;

 D_{frac} = diameter of the specimen's reduced parallel section after fracture;

 D_0 = diameter of the specimen's reduced parallel section prior to loading;

 $E_{\langle n,m\rangle}$ = initial elastic modulus: n = nominal, m = measured;

F = load cell force;

 $f_{y < n,m>}$ = initial yield stress: n = nominal, m = measured;

LP<#>= load protocol # as defined in de Castro e Sousa et al. (2020);

 $L_{extenso}$ = extensometer gauge length;

 N_T = number of experiments in a dataset;

 N_{ds} = number of data points in an experiment after downsampling;

 N_{orig} = number of data points in an experiment prior to downsampling;

t = time:

 $\delta_{extenso}$ = extensometer displacement;

 ε = true strain;

 ε_{eng} = engineering strain;

 ε_{frac} = average true strain across the necked specimen;

 $\dot{\varepsilon}$ = strain rate;

 μ = mean value;

 σ = true stress; and

 σ_{enq} = engineering stress.

References

- ASTM. 2015. Standard specification for structural steel shapes. ASTM A992/A992M-11. West Conshohocken, PA: ASTM.
- ASTM. 2016a. Standard practice for verification and classification of extensometer systems. ASTM E83-16. West Conshohocken, PA: ASTM.
- ASTM. 2016b. Standard specification for general requirements for rolled structural steel bars, plates, shapes, and sheet piling. ASTM A6/A6M-16a. West Conshohocken, PA: ASTM.
- ASTM. 2016c. Standard test methods for tension testing of metallic materials. ASTM E8/E8M-16a. West Conshohocken, PA: ASTM.
- ASTM. 2017. Standard test method for Young's modulus, tangent modulus, and chord modulus. ASTM E111-17. West Conshohocken, PA: ASTM.
- ASTM. 2018. Specification for cold-formed welded and seamless carbon steel structural tubing in rounds and shapes. ASTM A500/A500M-18. West Conshohocken, PA: ASTM.
- ASTM 2021. Standard practices for force verification of testing machines. ASTM E4-21. West Conshohocken, PA: ASTM.
- Braconi, A., et al. 2013. Optimising the seismic performance of steel and steel-concrete structures by standardising material quality control (OPUS). Luxembourg, UK: European Commission Research Fund for Coal and Steel.
- CEN (European Committee for Standardization). 2005a. *Designation* system for steels—Part 1: Steel names. EN 10027-1:2005. Brussels, Belgium: CEN.
- CEN (European Committee for Standardization). 2005b. Eurocode 3: Design of steel structures—Part 1-1: General rules and rules for buildings. EN 1993-1-1. Brussels, Belgium: CEN.
- CEN (European Committee for Standardization).2005c. Hot rolled products of structural steels—Part 2: Technical delivery conditions for non-alloy structural steels. ASTM EN 10025-2. Brussels, Belgium: CEN.
- CEN (European Committee for Standardization). 2019a. Hot rolled products of structural steels—Part 3: Technical delivery conditions for normalized/normalized rolled weldable fine grain structural steels. NF EN 10025-3. Brussels, Belgium: CEN.
- CEN (European Committee for Standardization). 2019b. Hot rolled products of structural steels—Part 6: Technical delivery conditions for flat products of high yield strength structural steels in the quenched and tempered condition. NF EN 10025-6:2019. Brussels, Belgium: CEN.
- Chaboche, J. L., K. D. Van, and G. Cordier. 1979. "Modelization of the strain memory effect on the cyclic hardening of 316 stainless steel." In *Proc.*, 5th Int. Conf. on Structural Mechanics in Reactor Technology. Berlin: North-Holland Publishing.
- Chang, G. A., and J. B. Mander. 1994. Seismic energy based fatigue damage analysis of bridge columns. Part 1—Evaluation of seismic capacity. Rep. No. NCEER-94-0006. Buffalo, NY: National Center for Earthquake Engineering Research.
- Cooke, R., and A. Kanvinde. 2015. "Constitutive parameter calibration for structural steel: Non-uniqueness and loss of accuracy." *J. Constr. Steel Res.* 114 (Nov): 394–404. https://doi.org/10.1016/j.jcsr.2015.09.004.
- Dafalias, Y. F., and E. P. Popov. 1975. "A model of nonlinearly hardening materials for complex loading." Acta Mech. 21 (3): 173–192. https://doi. org/10.1007/BF01181053.
- de Castro e Sousa, A., A. R. Hartloper, and D. G. Lignos. 2019. "RESSPy-Lab: Python tools for structural steel research, version 1.1.6." Accessed August 26, 2022. https://github.com/AlbanoCastroSousa/RESSPyLab.

- de Castro e Sousa, A., Y. Suzuki, and D. Lignos. 2020. "Consistency in solving the inverse problem of the voce-chaboche constitutive model for plastic straining." *J. Eng. Mech.* 146 (9): 04020097. https://doi .org/10.1061/(ASCE)EM.1943-7889.0001839.
- Deierlein, G. G., and A. Zsarnóczay. 2019. State-of-art in computational simulation for natural hazards engineering. Rep. No. 2019-01. Richmond, CA: NHERI SimCenter.
- Douglas, D. H., and T. K. Peucker. 1973. "Algorithms for the reduction of the number of points required to represent a digitized line or its caricature." *Cartographica: Int. J. Geogr. Inf. Geovisualization* 10 (2): 112–122. https://doi.org/10.3138/FM57-6770-U75U-7727.
- El Jisr, H. 2022. "The role of the composite floor system and framing action in the seismic performance of composite steel moment-resisting frames." Ph.D. thesis, School of Architecture, Civil and Environmental Engineering, École Polytechnique Fédérale de Lausanne.
- Filippou, F. C., E. P. Popov, and V. V. Bertero. 1983. Effects of bond deterioration on hysteretic behavior of reinforced concrete joints. Rep. No. UCB/EERC-83/19. Richmond, CA: Earthquake Engineering Research Center, Univ. of California, Berkeley.
- Garcia, M. A. R. 2020. "Multiaxial fatigue analysis of high-strength steel welded joints using generalized local approaches." Ph.D. thesis, School of Architecture, Civil and Environmental Engineering, École Polytechnique Fédérale de Lausanne.
- Grigoriou, V., and D. G. Lignos. 2017. Characterization of the cyclic hardening properties of European steels. Lausanne, Switzerland: Resilient Steel Structures Laboratory, École Polytechnique Fédérale de Lausanne.
- Hajjar, J. F., P. H. Schiller, and A. Molodan. 1998. "A distributed plasticity model for concrete-filled steel tube beam-columns with interlayer slip." *Eng. Struct.* 20 (8): 663–676. https://doi.org/10.1016/S0141-0296(97) 00107-7.
- Hartloper, A. R. 2022. "rlmtp: RESSLab Material Test Processing, version 1.0.0." Accessed August 26, 2022. https://github.com/ahartloper/rlmtp.
- Hartloper, A. R., A. de Castro e Sousa, and D. G. Lignos. 2021. "Constitutive modeling of structural steels: Nonlinear isotropic/kinematic hardening material model and its calibration." *J. Struct. Eng.* 147 (4): 04021031. https://doi.org/10.1061/(ASCE)ST.1943-541X.0002964.
- Hartloper, A. R., S. Ozden, A. de Castro e Sousa, and D. G. Lignos. 2022. "Database of uniaxial cyclic and tensile coupon tests for structural metallic materials, version 1.0.0." Accessed August 26, 2022. https://zenodo.org/record/6965147.
- Heredia Rosa, D. I., A. R. Hartloper, A. de Castro e Sousa, D. G. Lignos, M. Motavalli, and E. Ghafoori. 2021. "Experimental behavior of ironbased shape memory alloys under cyclic loading histories." *Constr. Build. Mater.* 272 (Feb): 121712. https://doi.org/10.1016/j.conbuildmat .2020.121712.
- Inamasu, H., A. de Castro e Sousa, and D. G. Lignos. 2022. "Development and experimental validation of dissipative embedded column base connections for enhanced seismic performance of steel moment-resisting frames." J. Struct. Eng. 148 (3): 04021280. https://doi.org/10.1061 //ASCE)ST.1943-541X.0003259.
- JISC (Japanese Standards Association). 2014. Dimensions, mass and permissible variations of hot rolled steel sections. JIS G 3192:2014. Tokyo, Japan: JISC
- Kent, D. C., and R. Park. 1971. "Flexural members with confined concrete." J. Struct. Div. 97 (7): 1969–1990. https://doi.org/10.1061/JSDEAG .0002957.
- Ozden, S. 2021. "Experimental investigation of the cyclic properties of welds in mild structural steels." M.S. thesis, School of Architecture, Civil and Environmental Engineering, École Polytechnique Fédérale de Lausanne.
- Ramer, U. 1972. "An iterative procedure for the polygonal approximation of plane curves." *Comput. Graphics Image Process.* 1 (3): 244–256. https://doi.org/10.1016/S0146-664X(72)80017-0.
- Sadowski, A. J., J. M. Rotter, T. Reinke, and T. Ummenhofer. 2015. "Statistical analysis of the material properties of selected structural carbon steels." *Struct. Saf.* 53 (Mar): 26–35. https://doi.org/10.1016/j.strusafe.2014 .12.002.

- Skiadopoulos, A. 2022. "Welded moment connections with highly dissipative panel zones for enhanced seismic performance of steel moment frames." Ph.D. thesis, School of Architecture, Civil and Environmental Engineering, École Polytechnique Fédérale de Lausanne
- Suzuki, T., Y. Yoshida, Y. Shimura, Y. Suzuki, S. Kubota, and M. Nagata. 2008. Development of building structural steel with high yield ratio and
- high yield point leading to innovative steel structural system. Rep. No. 97. Tokyo: Nippon Steel.
- Suzuki, Y., and D. G. Lignos. 2021. "Experimental evaluation of steel columns under seismic hazard-consistent collapse loading protocols." J. Struct. Eng. 147 (4): 04021020. https://doi.org/10.1061/(ASCE)ST.1943-541X.0002963.
- Voce, E. 1948. "The relationship between stress and strain for homogeneous deformation." *J. Inst. Met.* 74: 537–562.